UC Berkeley
UC Berkeley Previously Published Works

Title

Kinetics and mechanism of heterogeneous voltage-driven water-dissociation catalysis

Permalink

Journal

ISSN

Authors

Chen, Lihaokun
Xu, Qiucheng
Boettcher, Shannon W

Publication Date

DOI

Peer reviewed

Kinetics and Mechanism of Heterogeneous Voltage-Driven Water-Dissociation Catalysis

Lihaokun Chen[1], Qiucheng Xu[1,2], Shannon W. Boettcher[1*]

[1] Department of Chemistry and the Oregon Center for Electrochemistry, University of Oregon, Eugene,

Oregon 97403, United States

[2] Present: Surface Physics and Catalysis (Surf Cat) Section, Department of Physics, Technical University

of Denmark, 2800 Kgs. Lyngby, Denmark

To whom correspondence should be addressed:

*swb@uoregon.edu

SUMMARY

The water-dissociation reaction (WD, $H_2O \rightarrow H^+ + OH^-$) affects the rates of electrocatalytic reactions and the performance of bipolar membranes (BPMs). How catalyzed interfacial WD is driven by voltage, however, is not understood. We designed a BPM electrolyzer with two reference electrodes attached laterally to each layer/side (here, poly(arylpiperidinium) and perfluorosulfonic-acid ionomers) to measure WD current and overpotential (η_{wd}), without soluble electrolyte and as a function of temperature and catalyst-layer properties. Using TiO_2-P25 nanoparticles as a model WD catalyst, Arrhenius-type analysis yields a WD activation energy E_a of 25–30 kJ mol^{-1}, only weakly dependent η_{wd}. The pre-exponential factor is unexpectedly proportional to η_{wd}. With D_2O, η_{wd} is ~2 to 4 times larger than in H_2O, largely due to a lower pre-exponential factor. Without catalyst, η_{wd} is ~10-fold larger and E_a decreases from 34 to 24 kJ mol^{-1} as η_{wd} goes from 0.1 to 1 V. To explain these data, we propose a new WD mechanism where metal-oxide nanoparticles, polarized by the voltage across the BPM junction, serve as *i*) proton acceptors (from water) on the negative sides of the particle to generate free OH^-, *ii*) proton donors on the positive sides to generate H_3O^+, and *iii*) surface proton conductors that connect spatially separate donor/acceptor sites. Increasing electric-field strength with overpotential orients water for proton-transfer elementary steps comprising WD, increasing the pre-exponential factor and hence rate, but is insufficient to lower E_a. This understanding will accelerate development of electrocatalysis, electrodialysis, carbon-capture, and carbon-utilization technologies that require efficient WD.

CONTEXT & SCALE

Water dissociation (WD, $H_2O \rightarrow H^+ + OH^-$) is one of the most-important reactions in chemistry. The rate of WD controls the performance of bipolar membranes (BPMs), which can convert electrical energy into acid and base solutions for water treatment or for direct-air or ocean-based CO_2 capture and interfacial electrocatalysis reactions that are central to renewable electrical-energy storage like the reduction of water to H_2 and CO_2 to fuels. We report new method to accurately measure the voltage required to drive WD as a function of temperature using a BPM water-electrolyzer platform, and illustrate a fundamentally new model for how the WD reaction can be catalyzed by nanoparticle surfaces able to donate, accept, and transport protons.

INTRODUCTION

When water is consumed as a reactant in chemical and (electro)catalytic processes, water dissociation (WD, $H_2O \quad H^+ + OH^-$), is often a critical elementary step. In a bipolar membrane (BPM), for example, water is dissociated at the junction between an ionomer anion-exchange layer (AEL) and cation-exchange layer (CEL), usually accelerated by a catalyst sandwiched between the two and driven by an applied voltage (**Figure 1a**) [1-5]. This catalyzed, voltage-driven WD process is not understood, even though BPMs are used in electrodialysis to produce acid/base from brine and to desalinate water [6-9], in food processing to adjust pH [10], and in a variety of recycling and separations processes [11]. BPMs can also couple different-pH microenvironments leading to novel uses in fuel cells [12,13], flow batteries [14] and water [15,16] and CO_2 electrolyzers [17-19] that can be impurity-tolerant [20] and enable the use of efficient and abundant electrocatalysts. WD, likely voltage-driven in an electrochemical double layer and accelerated via surface reactions, is also likely a key elementary step in electrocatalytic reactions including hydrogen evolution and CO_2 reduction

that require protons in neutral-to-basic media where few protons are available [15,21-23].
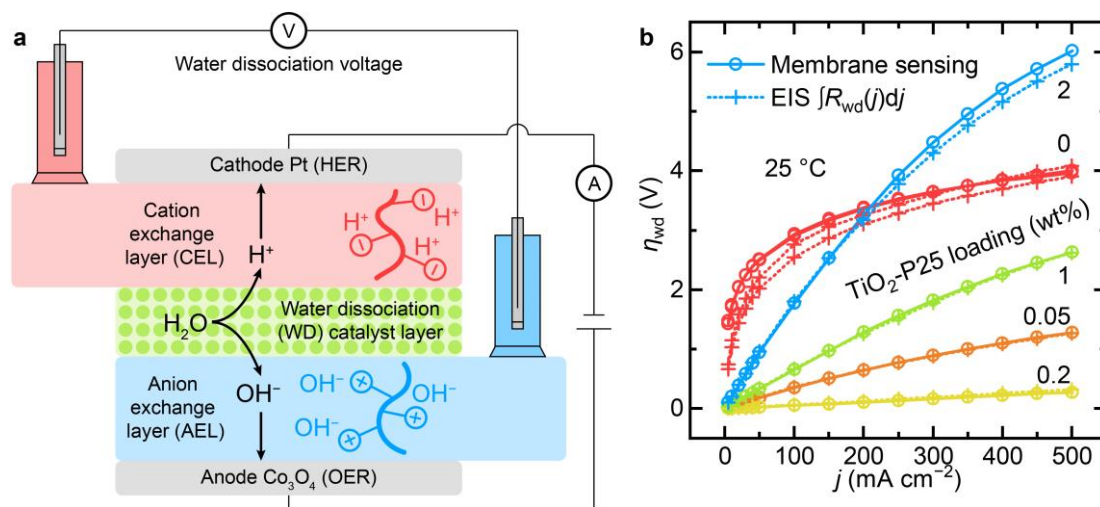

Figure 1. (a) Schematic of membrane-potential-sensing in a bipolar membrane (BPM) electrolyzer. In the AEL, positive functional groups (e.g. quaternary ammonium cations) are fixed to the polymer backbone while small anions like OH^- are mobile. In the CEL, negative groups (e.g. sulfonate) are fixed to the polymer backbone and small cations like H^+ are mobile. Pure water is fed to cathode and anode gas-diffusion electrodes and diffuses to the BPM. WD occurs at the junction of the AEL and CEL. The voltage between the two reference electrodes connected to the AEL and CEL by membrane strips was recorded as a function of applied current. By subtracting the values at open circuit, the WD overpotential η_{wd} is calculated. **(b)** Comparison between the electrochemical-impedance-spectroscopy (EIS) and membrane-potential-sensing methods of determining η_{wd}. The impedance spectra from the entire cell were measured at different current densities j. The WD resistances R_{wd} were extracted by fitting the spectra and η_{wd} was calculated by integrating R_{wd} as a function of j. Loading is represented by the spin-coat ink concentration; 0.2 wt% yields ~10 μg cm^{-2} or ~200 nm thick nanoparticle films.

The efficiency of WD is central to the performance of BPMs. We recently showed that metal-oxide nanoparticles dramatically accelerate the WD reaction both in bipolar membranes and as a step in electrocatalysis [15], and that the ability of the WD catalyst to screen and focus the interfacial electric field in the BPM junction is important [24]. Previously either an electric-field effect (so-called second Wien effect) [25-28], a catalytic effect [15,29,30], or a combination of two [24,31,32] has been invoked to explain WD kinetics in the BPM orders of magnitude faster than the equilibrium rates in bulk water, but how field and catalysis interact

at the microscopic/mechanistic level is unknown.

These previous studies are also limited in how they assess the WD voltage, usually in H-cells or multi-compartment cells with supporting electrolytes that contain salt ions (other than H^+ and OH^-) such as Na^+ and Cl^- where the current carried by salt ions complicates the analysis of the polarization curves and the study of WD and with unknown contribution from series resistance. Temperature-dependent kinetics are central to understand mechanisms and extract activation energies (E_a), but these are rarely done for BPMs due to the experimental difficulties in isolating the WD overpotential voltage (the thermodynamic driving force for WD) [15] from other temperature-dependent processes. The few previous studies have found widely ranging apparent activation energies from ~10-80 kJ mol^{-1}, primarily measured for commercial BPMs where the interface chemistry and structure where WD occurs are unknown. [29,33-37] The WD rate constant also depends on the pre-exponential factor A, which is not seldom discussed in the above, as is unfortunately typical in electrochemistry [37].

We previously avoided these complications by using BPMs in a pure-water electrolyzer, without salt ions, where H^+ and OH^- are the only ionic charge carriers [15,38]. We also have demonstrated that the (areal) WD resistance R_{wd} can be isolated from the total impedance (that includes electrode reaction and transport) via electrochemical impedance spectroscopy (EIS) [24]. The WD overpotential/overvoltage η_{wd} is calculated from R_{wd} by

$$\eta_{wd} = \int_0^j R_{wd}(j)\mathrm{d}j \tag{1}$$

where j is the current density. R_{wd} is a differential resistance that is a function of j (or equivalently, η_{wd}, the driving force for WD). R_{wd} decreases with driving force and thus j. When R_{wd} does not depend on j, Eq. 1 reduces to Ohm's law. Estimating η_{wd} in this way requires measuring EIS at different j, which is slow due to the need for low-frequency data. Some BPMs change during testing, making it difficult to separate

temperature-dependent kinetics from other processes. In Nyquist plots, the WD semicircle is sometimes not well-separated and low-frequency inductive loops can appear, complicating the analysis and introducing error.

Here we report a new method – termed "membrane-potential-sensing" – to directly measure η_{wd} in BPM electrolyzers as a function of temperature and current, and use the method to discover new underlying physical processes controlling WD rate. We used a simpler setup in anion-exchange-membrane electrolyzers to separate the anode and cathode voltage with one reference electrode [39], as reported for fuel cells as well [40-42]. An AEL and a CEL membrane-sensing strip are connected to the AEL and CEL of the BPM, respectively (**Figure 1a**), with separate reference electrodes attached to each strip. After subtracting the open-circuit values, η_{wd} is the voltage difference between the two references (ohmic drop across AEL and CEL is small and can be ignored). We demonstrate that η_{wd} measured by membrane-potential sensing is almost identical to that from EIS, corroborating both approaches. We use the method to study temperature-dependent WD kinetics on model TiO_2-P25 catalyst. We discover that while uncatalyzed BPMs show decreasing E_a with driving force, as with typical electrode-kinetics models such as Butler-Volmer, WD in catalyzed BPMs has an apparent E_a that is almost independent of η_{wd}, but a pre-exponential factor A that surprisingly increases linearly with η_{wd}. We develop a semi-empirical "BPM equation" to quantitatively describe the temperature-dependent kinetics based on the equilibrium activation energy $E_{a,0}$, the effective proton-transfer coefficient α (to describe the effect of η_{wd} on the activation barrier), and a pre-exponential factor A that depends linearly on η_{wd}. Kinetic-isotope experiments show that BPMs fed D_2O have higher η_{wd} than H_2O, with similar E_a and different A. Adding electronically conducting acetylene carbon black (ACB) to a thick layer of TiO_2-P25 both lowers E_a and increases the sensitivity of E_a on η_{wd}, supporting the hypothesis that the electric field is concentrated by conductors to increase WD kinetics. We propose a new mechanism of field/voltage-driven

WD catalysis that includes field-dependent organization of surface water, proton transport from/to surface water to/from the metal oxide WD catalyst, and proton transport on/across the catalyst nanoparticle surface.

RESULTS AND DISCUSSION

Comparison between membrane-potential-sensing and EIS methods. Previously we showed that EIS can be used to isolate the WD resistance R_{wd} from the total-cell impedance (**Figure S1**) [24]. In a Nyquist plot, the high-frequency semicircle is related to WD while the low-frequency semicircles are related to anode and cathode charge-transfer resistances and capacitances. Fitting to equivalent circuits is used to extract R_{wd}. for each different j. Integrating R_{wd} as a function of j, we calculate $\eta_{wd} = \int_0^j R_{wd}(j)dj$. To corroborate the membrane-potential-sensing and EIS methods, we compare the two ways to calculate η_{wd} for the same sample (**Figure 1b**). The methods produce similar $\eta_{wd} - j$ curves, regardless of WD catalyst loadings. Because the EIS measurement is slow, making degradation effects more serious and complicating the temperature-dependence measurement, we use the data from membrane-potential sensing in the analysis below.

Temperature dependence and Arrhenius analysis. The WD polarization curves with different TiO$_2$-P25 loadings from 25–55 °C are shown in **Figure 2** and **Figure S2**. We chose TiO$_2$-P25 as the model catalyst due to its abundance, low cost, and good performance as a single-composition catalyst in BPM electrolyzers. The optimal loading is 0.2 wt% (represented by the spin-coat ink concentration and equivalent to ~10 μg cm^{-2} and ~200 nm in thickness) [24]. In pristine BPMs without WD catalyst, j increases exponentially with η_{wd}, like a typical electrochemical reaction with Tafel-like behavior (or Marcus / Butler-Volmer behavior, which are fundamentally related). In contrast, BPMs with optimal loading of TiO$_2$-P25 show a linear dependence of j on η_{wd}, more like a resistor that follows Ohm's law. Polarization curves of other loadings lie

between these two cases, i.e., with a (nearly) linear shape when η_{wd} is small and more exponential when η_{wd} is large. The linear relationship is analogous to the limiting case of the Butler-Volmer model when the exchange current density j_0 is large, or in other words, fast electrode charge transfer kinetics and only a small overpotential η is needed to drive a large current density (see discussion below).
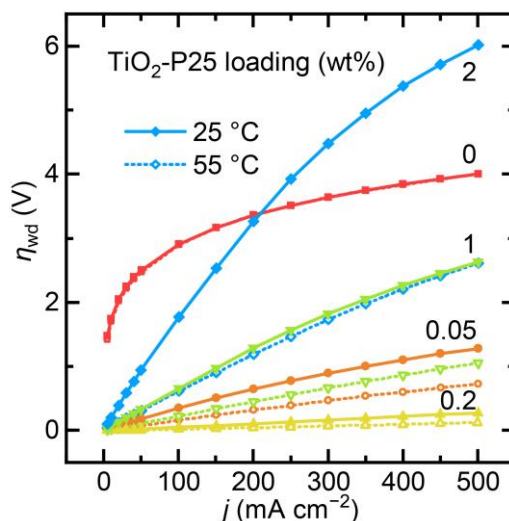

Figure 2. Temperature-dependent polarization curves of BPMs with different mass loadings of TiO$_2$-P25 WD catalyst showing transition from exponential to linear $j - \eta_{wd}$ response with increasing loading. Temperatures tested were 25, 35, 45, and 55 ± 2 °C, but only data at 25 and 55 °C are shown here for clarity. The uncatalyzed BPM (labelled 0) has almost no apparent temperature dependence at the high current densities tested here due to concomitant degradation processes.

Increasing the temperature lowers η_{wd} in most cases, except for the BPM without catalyst. This artifact was because the pristine uncatalyzed BPM performance degrades during testing, obscuring the temperature dependence. Therefore, for pristine BPM data reported below, we use only low current densities and a small correction for the calibrated degradation rate (**Figure S3**). To analyze the data from BPMs with and without WD catalysts we use an Arrhenius-type model

$$j = Ae^{-\frac{E_a}{RT}} \tag{2}$$

where A is the pre-exponential factor, E_a is the apparent activation energy, R is the gas constant, and T is the temperature. Notice A has the same unit as j (mA cm^{-2}). Since the concentration of the reactant, i.e., water,

is unknown inside the BPM junction, we did not normalize A to unit concentration [37]. We assume the concentration of water is largely constant as we apply ≤ 500 mA cm^{-2}, significantly above which water transport into the BPM can be limiting [38]. Our aim is to analyze E_a and A at a fixed η_{wd} (but not j) since η_{wd} represents the driving force while j the WD reaction rate—there are no salt ions to otherwise carry current so all measured current must be associated with WD. Because we collect data under current control, the $j - \eta_{wd}$ data are interpolated with cubic splines (**Figure 3a**). For a fixed η_{wd}, the interpolated $\ln j$ is plotted against $1/T$ to generate Arrhenius plots. The slope and vertical intercept from linear fits yield E_a and A, respectively. The procedure is repeated for different η_{wd} (**Figure 3b**) to understand how the driving force for WD modulates kinetics and possible mechanisms. The slope does not change with $1/T$ (within the temperature range of the experiment); E_a and A are thus independent of T. In the next section we discuss how E_a and A depend on η_{wd} and WD catalyst loading, as this informs the microscopic picture of catalyzed WD reactions in BPMs, and more broadly in electrocatalysis where reactions also take place in the presence of large interfacial electric field [22,43,44].
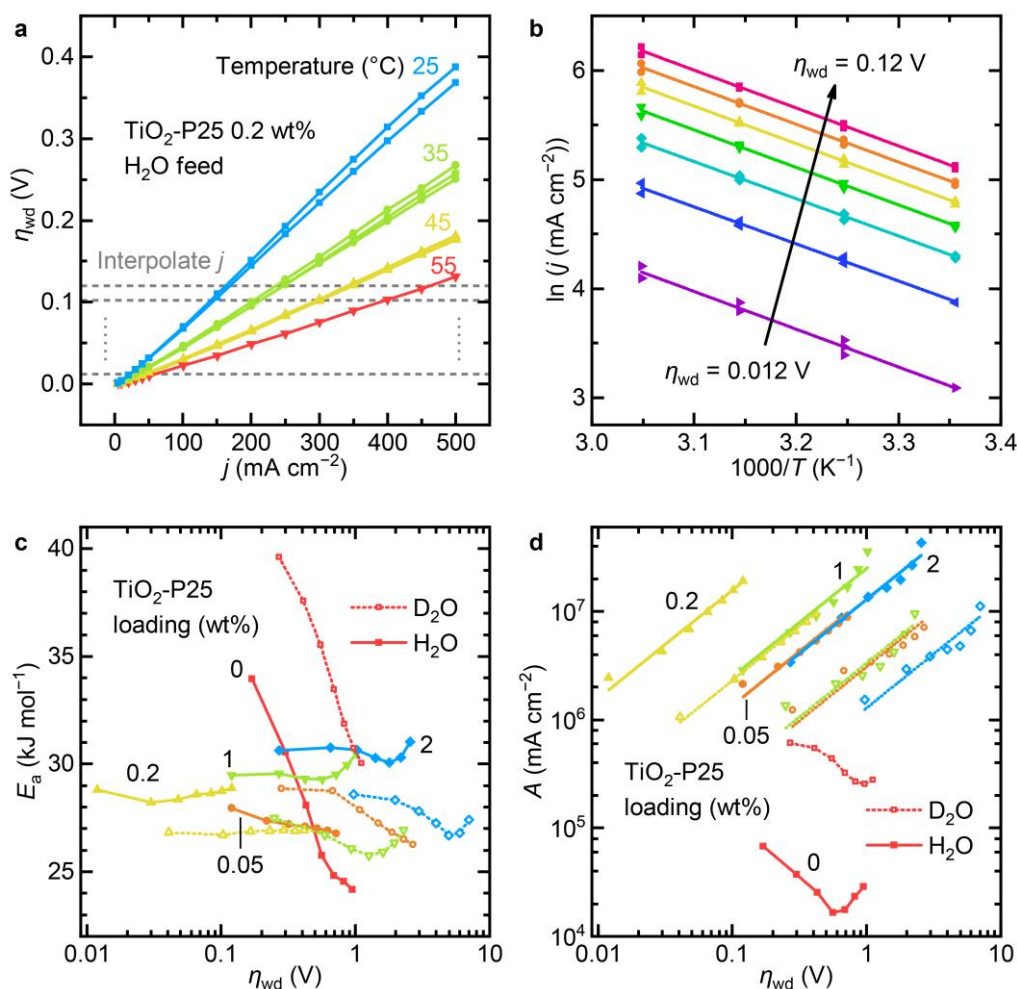
Figure 3. Arrhenius analysis of temperature-dependent BPM polarization curves. **(a)** Temperature-dependent polarization curves of a BPM with 0.2 wt% TiO₂-P25 and fed by H₂O. The same sample is cycled between 25 and 55 °C. Current density j is interpolated at certain η_{wd}. **(b)** Arrhenius plots of a BPM with 0.2 wt% TiO₂-P25 and fed by H₂O at different η_{wd}'s. Lines are least-squares linear fits of the experimental data. **(c)** Apparent activation energy E_a as a function of η_{wd}. Different loadings of TiO₂-P25 are used as WD catalyst. The electrolyzer is fed by either H₂O or D₂O. Notice the log scale on the horizontal axis. **(d)** The pre-exponential factor A as a function of η_{wd}. Notice the log scale on both axes. Lines are least-squares linear fits with fixed slope of one except the loading of 0. Voltage increases the pre-exponential factor for catalyzed samples instead of lowering the activation barrier.

Overpotential and mass-loading dependence of kinetic parameters. The apparent E_a and A as a function of η_{wd} with different TiO₂-P25 loadings are shown in **Figure 3c**. For the pristine BPM without WD catalyst, E_a decreases from 34 to 24 kJ mol^{-1} as η_{wd} increases from 0.2 to 1 V. This behavior is like those observed for interfacial faradaic processes, where the activation energy for electron transfer (e.g., in the Butler-Volmer

or Marcus models) is lowered with increasing absolute overpotential. For BPMs with TiO_2-P25 catalyst, however, E_a is essentially constant with η_{wd}. The similar independence of E_a on transmembrane voltage has also been observed occasionally in other studies of BPMs, as mentioned above [29,35].

Differences in WD process in BPMs compared with WD in pure water are also apparent (**Table 1**). In pure water, Eigen and de Maeyer determined the apparent E_a for WD $E_a(k_D) = 64.9$–69.0 kJ mol^{-1} while for neutralization $E_a(k_R) = 8$–13 kJ mol^{-1}, where k_D and k_R denote the rate constant of WD and H$^+$/OH$^-$ recombination/neutralization respectively [45,46]. Natzle and Moore found $E_a(k_R) = 15 \pm 3$ kJ mol^{-1} [47]. Since $E_a(k_D)$ and $E_a(k_R)$ are related by the standard enthalpy of WD as $\Delta H° = E_a(k_D) - E_a(k_R) = 56$ kJ mol^{-1} [48,49], and thus $E_a(k_D) = 71 \pm 3$ kJ mol^{-1}, which is comparable with the results of Eigen and de Maeyer. Interestingly, the E_a for WD in BPMs is lower than $E_a(k_D)$ in pure water by a factor of two, suggesting a different mechanism and/or solvation environment.

Unexpectedly, we find that the pre-exponential factor A increases almost linearly with η_{wd} for catalyzed BPMs (**Figure 3d**, notice the log–log scale and the unit-slope lines), in contrast with classic Butler-Volmer models where E_a decreases linearly with η, and A is independent of η [37]. We discuss a microscopic physical picture that may explain this behavior below.

Table 1. Kinetic and thermodynamic parameters of H₂O and D₂O dissociation

	H$_2$O	D$_2$O	H/D
Dissociation rate constant k_D (10^{-5} s^{-1})	2.5 [46]; 2.56 [50]; 2.04 [47]	0.25 [50]; 0.186 [47]	~11
Apparent activation energy $E_a(k_D)$ (kJ mol^{-1})	64.9–69.0 [46]	76* [50]	~0.88
Neutralization rate constant k_R (10^{11} M^{-1} s^{-1})	1.4 [46]; 1.43 [50]; 1.12 [47]	0.84 [50]; 0.741 [47]	~1.7
Apparent activation energy $E_a(k_R)$ (kJ mol^{-1})	8–13 [46]; 15 [47]	15* [50]	~0.85
Dissociation constant K_w (10^{-14})	1.0 [49]	0.11 [49]	~9.1
$\Delta G°$ (kJ mol^{-1})	79.87 [49]	85.23 [49]	~0.94
$\Delta H°$ (kJ mol^{-1})	55.82 [49]	60.87 [49]	~0.92
$\Delta S°$ (J mol^{-1} K^{-1})	−80.67 [49]	−81.75 [49]	~0.97

* Extracted from Arrhenius analysis using the literature values.

The BPM equation. The above Arrhenius analysis based on interpolation and linear fitting is limited by the η_{wd} of the highest test temperature (e.g., 0.12 V in **Figure 3a**), as above that there are only data of three

temperatures or fewer. We thus developed a semi-empirical equation to fit all the data and minimize the errors due to interpolation. We hypothesize, following the Butler-Volmer model, that

$$E_a = E_{a,0} - \alpha F \eta_{wd} \tag{3}$$

where $E_{a,0}$ is the "equilibrium activation energy" and $\alpha \geq 0$ is the "proton-transfer coefficient", a unitless number which describes how E_a for proton transfer changes with η_{wd} and determines the shape of the polarization curve. An α tending to 0 results in a linear $j - \eta_{wd}$ response (e.g., with optimal TiO_2-P25 loading) while a larger α leads to an exponential shape (e.g., as for the pristine BPMs). Because A is proportional to η_{wd}, we have

$$A = G_0 \eta_{wd} \tag{4}$$

where the new constant $G_0 = A/\eta_{wd}$ has the unit of areal conductance (mS cm^{-2}). Substituting these relations into the Arrhenius equation yields a semi-empirical "BPM equation" to describe WD in BPMs (the forward and reverse reaction contributions are not separated explicitly, see more discussion below)

$$j_{wd} = G_0 \eta_{wd} e^{-\frac{E_{a,0} - \alpha F \eta_{wd}}{RT}} = \left(G_0 e^{-\frac{E_{a,0}}{RT}} \right) \eta_{wd} e^{\frac{\alpha F \eta_{wd}}{RT}} \tag{5}$$

where G_0, $E_{a,0}$ and α depend on catalyst type and loading. By fitting j as a function of η_{wd} at different T, we extract the parameters G_0, $E_{a,0}$ and α using the entire data set (**Figure 4**). For most polarization curves, the fitting provides $R^2 > 0.99$ and the parameter-fitting errors are usually less than 10% of the parameter values (**Figure S2**). The fit requires variable-temperature polarization curves, since at a fixed T and with fixed catalyst and loading, G_0 and $E_{a,0}$ are interdependent and lumped into the term as $G_0 e^{-\frac{E_{a,0}}{RT}}$. At small η_{wd}, $e^{\frac{\alpha F \eta_{wd}}{RT}} \to 1$ and the linearized BPM equation is

$$j_{wd} = \left(G_0 e^{-\frac{E_{a,0}}{RT}} \right) \eta_{wd} \tag{6}$$

The classical linearized Butler-Volmer equation at small overpotential η provides

$$j_{BV} = \left(\frac{j_{0,BV} F}{RT} \right) \eta \tag{7}$$

In analogy with Eq. 6, we can define a WD exchange current density j_0

$$j_{0,wd} = \frac{RT}{F} G_0 e^{-\frac{E_{a,0}}{RT}} \tag{8}$$

Higher G_0 and lower $E_{a,0}$ give a larger j_0, and j_0 increases with temperature. The parameter G_0 can be called the driving-force-independent "proton-transfer conductance" and is likely related to the number of active proton acceptor/donor sites on the WD catalyst surface and the frequency by which water molecules interact with those sites to accommodate proton transfer (see below).
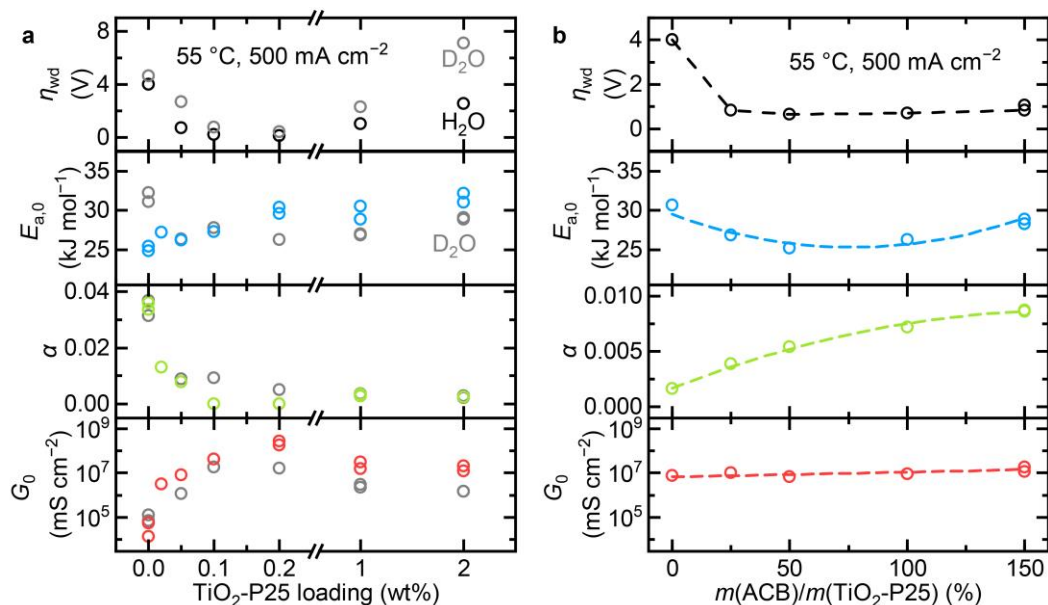

Figure 4. Temperature-dependence analysis using the semi-empirical BPM equation, $j_{wd} = G_0 \eta_{wd} e^{-\frac{E_{a,0} - \alpha F \eta_{wd}}{RT}}$, where $E_{a,0}$ is the "equilibrium activation energy", α is the "proton-transfer coefficient", and G_0 is the "proton-transfer conductance". To compare with BPM performance, η_{wd} at 55 °C and 500 mA cm^{-2} is also included. Notice the log scale on the vertical axis for G_0. **(a)** Different loadings of TiO$_2$-P25 are used as WD catalyst. The electrolyzer is fed by either H$_2$O or D$_2$O. Notice the log scale on the horizontal axis. **(b)** Different mass ratios of acetylene carbon black (ACB) and TiO$_2$-P25 are used as WD catalyst. The mass of TiO$_2$-P25 is kept constant while the mass of ACB is varied. The electrolyzer is fed by H$_2$O. The increase of the proton-transfer coefficient α with conductive additive is consistent with electric-field screening and focusing. Lines serve as a guide for the eye.

The parameters G_0, $E_{a,0}$ and α depend on TiO$_2$-P25 loading. $E_{a,0}$ increases from ~25 to ~30 kJ mol^{-1} from the BPM without catalyst to one with optimal loading (0.2 wt%, ~10 µg cm^{-2} and ~200 nm) then increases slowly and approaches $E_{a,0}$ ~32 kJ mol^{-1} when the loading is higher than 1 wt% (**Figure 4a**). The

shape of the polarization curve is related to α (compare **Figure 2** and **Figure 4a**). A smaller α results in a linear $j - \eta_{wd}$ response, as in the case for optimal loading ($\alpha = 0$), while a larger α yields a more-exponential dependence, as in the very low loadings and without catalyst. Interestingly, G_0 increases substantially with TiO$_2$-P25 loading before the optimal value (notice the log scale), and then slightly decreases. Lower $E_{a,0}$, higher α, and higher G_0 lead to a better performance. In the case of TiO$_2$-P25, G_0 appears to be the dominant factor and is correlated with η_{wd} (**Figure 4a**, top and bottom panels).

Kinetic isotope effects. To obtain information on the rate-limiting step in WD, we fed the BPM electrolyzer with D$_2$O and measured kinetic isotopic effects (**Figure S4**). For the catalyzed BPMs, η_{wd} in D$_2$O is ~2 to 4 larger than in H$_2$O (**Figure 4a**, top panel) despite both $E_{a,0}$ and α being relatively similar in both. The larger η_{wd} in D$_2$O is largely due to a lower G_0 (and thus A), which is evident in **Figure 3d**. These isotope effects can be compared with those found for diffusion coefficients and associated activation energies for H$_2$O, D$_2$O, and their ions (**Table 2**). Diffusion of these species follows an Arrhenius model with an activation energy of $E_a(D)$. Although the diffusion coefficients show H/D ratios (defined as the value of H species relative to D species, such as H$_2$O/D$_2$O, H$^+$/D$^+$, and OH$^-$/OD$^-$) ranging from 1.2 to 1.7, the H/D ratios of $E_a(D)$ are close to unity. Bulk H$_2$O and D$_2$O also show different in dissociation kinetics (**Table 1**). Compared to D$_2$O, the dissociation equilibrium constant K_w and dissociation rate constant k_D of H$_2$O is 9 and 11 times larger, respectively, while both $E_a(k_D)$ are similar. These data are consistent with our experimental results of H$_2$O and D$_2$O in voltage-driven catalyzed WD reaction in the BPM; the rates/current densities are substantially slower for D$_2$O (characterized by A or G_0), but the temperature dependence (characterized by E_a) are similar. These data point to the pre-exponential factor A being associated not only with the number of catalyst proton acceptor/donor sites on the surface, but also with the facility by which water molecules can organize via molecular motion for the charge transfer step, as discussed more fully below.

Table 2. Diffusion coefficients and associated activation energies for H_2O, D_2O and their ions

	H_2O	D_2O	H/D
Diffusion coefficient D $(10^{-5}\ cm^2\ s^{-1})$	2.299 [51]	1.872 [51]	~1.2
Apparent activation energy $E_a(D)$ $(kJ\ mol^{-1})$	18–20 [51]	19–21 [51]	~0.95
	H^+	D^+	H/D
Diffusion coefficient D $(10^{-5}\ cm^2\ s^{-1})$	9.311 [52]	6.655 [52]	~1.4
Apparent activation energy $E_a(D)$ $(kJ\ mol^{-1})$	10.6 [53]; 10.0* [54]	10.0* [54]	~1
	OH^-	OD^-	H/D
Diffusion coefficient D $(10^{-5}\ cm^2\ s^{-1})$	5.273 [52]	3.169 [52]	~1.7
Apparent activation energy $E_a(D)$ $(kJ\ mol^{-1})$	13 [53]; 12.6* [54]	13.0* [54]	~1

*Activation energy of ionic conductivity is used due to the lack of data.

Effect of electronic conductivity. We previously showed that adding electronic conductors such as acetylene carbon black (ACB) nanoparticles to a thick layer (~120 μg cm^{-2} and ~2.4 μm) of TiO_2-P25 WD catalyst improves the BPM performance substantially, likely through focusing the electric at the AEL|catalyst and catalyst|CEL interfaces [24]. We measured the temperature dependence of these thick TiO_2-P25 WD layers mixed with different ratio of ACB (by mass) as WD catalyst. Adding ACB lowered η_{wd} (the optimal ratio is between 50% and 100%) consistent with previous results [24] (**Figure 4b**). Analysis of the new temperature-dependent data shows that adding ACB lowers $E_{a,0}$ from ~30 to ~26 kJ mol^{-1} when the mass ratio increases from 0 to 50%, and increases α by a factor of ~5 (from ~0.002 to ~0.09) when the mass ratio increases from 0 to 150%, but does not change G_0 significantly. Simpler Arrhenius analysis also shows that E_a is lowered (**Figure S5**), consistent with the BPM-equation analysis. Adding electronically conductive material to the region of WD thus appears to improve kinetics for thick catalyst layers by screening and increasing local-electric-field strength that serves to lower E_a with increasing applied voltage.
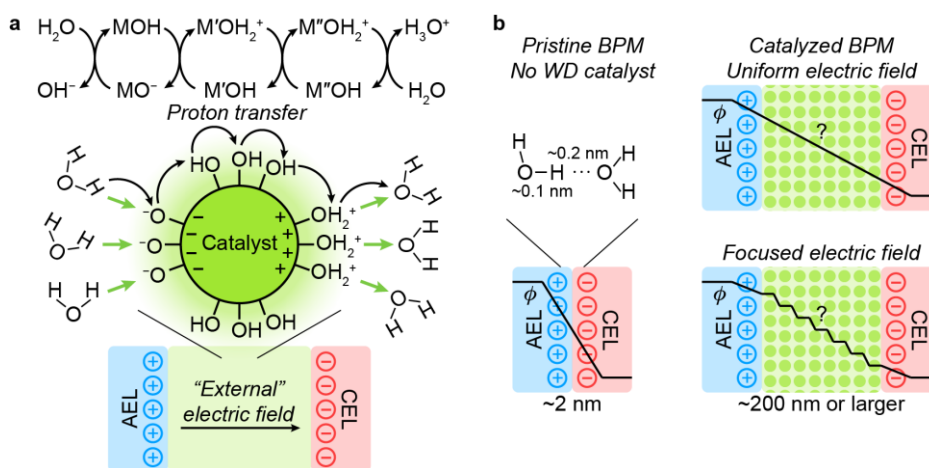
Figure 5. Proposed mechanism for voltage-driven catalyzed WD. (a) The "external" electric field originates from the unbalanced fixed charges in the AEL and CEL. The local electric field (shown in green arrows), originates from the protonation and deprotonation of the nanoparticle surface hydroxyls, and further modulated by electronic polarization inside the nanoparticles, as well as the external electric field. The local electric field induces the water molecules to orient facilitate WD and proton transfer. M, M′, and M″ denote different sites on the catalyst surface. **(b)** Possible electric-potential ϕ profiles of pristine BPMs and catalyzed BPMs. The hydrogen bond between water molecules is also shown for comparison.

A new microscopic model for voltage-driven catalyzed WD. The sum of the kinetic data and analysis lead us to propose a new tentative model for WD on metal-oxide surfaces (**Figure 5**) that is relevant not only for BPMs but also interfacial electrocatalytic processes where WD is required to provide protons, e.g., CO_2 or H_2O reduction in neutral to basic conditions [18]. Acid-base reactions, H^+ and OH^- transfer, and WD, all involve the interconversion between O–H and hydrogen bonds. The Grotthuss mechanism of H^+ and OH^- transport in water involves the movement of charge through a series of protonation and deprotonation of different water molecules (i.e., the interconversion between O–H bonds and hydrogen bonds, non-vehicular transport). Similar mechanisms can occur on the surface of oxide nanoparticles, due to the various species such as bridging and terminal oxo and hydroxyl groups that can be protonated or deprotonated and that interact strongly with interfacial water to mediate proton transport [55,56]. The surface of metal oxides thus may serve as a "sink" or "source" of protons which can transport on the nanoparticle surface through the surface oxo/hydroxyl groups. The oxide surface can thus serve as both proton reservoir and proton conductor.

Local equilibrium between the WD catalyst and liquid water further leads to interfacial electrostatic effects in the form of a double layer electric field whenever the local pH is not at the point of zero charge (PZC) of the nanoparticle. The strength of this local interfacial field is likely important for proton transfer reactions between the surface of the catalyst particle and the water, because the electric field modulates substantially interface-water structure and properties, like the effective dielectric constant and average orientation [57-59].

In the BPM junction, however, the situation is further affected by the *external* electric field originating from the uncompensated fixed charges at the AEL and CEL. If the nanoparticle has high electronic conductivity (e.g., IrO_x, $Sb:SnO_2$, etc.), the electrons inside the nanoparticle will redistribute to screen the electric field and the nanoparticle will be polarized, much like a nanoscale bipolar electrode [60]. These conductive catalysts could even drive faradaic reactions (such as electrolysis) if sufficiently polarized, but we note for our catalysts the applied WD overpotential is typically too low for such reactions to occur. WD catalysts with a high dielectric constant (e.g., TiO_2), will similarly screen the electric field inside the particle and increase the electric field outside the particle within the effective Debye length defined by the local conditions at particle surface [61].

In both high-dielectric and conductive particles, the polarization of the particle by the external electric field across the BPM enhances the local electric field near the nanoparticle surface, driving water molecules to orient and align, on average, their dipole moment with electric field [59]. Under reverse-bias operation, i.e., where the BPM is driving WD at the junction, the space charge regions in the AEL and CEL increase with applied bias leading to an increasing average electric-field strength across the WD catalyst layer and increasing the degree of water orientation.

We propose that the water organization at the WD catalyst/water interface, driven by the external

electric field, is responsible for the experimentally measured pre-exponential factor, representing an organization process that describes the fraction of time, and frequency by which, the system is poised for proton transfer. This new model explains the proportionality between A and η_{wd}. As the local electric field increases with η_{wd}, water molecules are, on average, better oriented for donating a proton to one side of the WD catalyst particle (i.e., partial-positive proton on H_2O pointed toward the surface) and accepting a proton on the other side of the WD catalyst (i.e., with the partial-negative O on H_2O pointed toward the surface), as depicted in **Figure 5a**. The fact that D_2O has a smaller A than H_2O is consistent with the slower vibrational frequency and molecular motions of heavier D_2O.

While the above argument provides an explanation for how the local electric field, both at equilibrium and increasing with applied reverse bias, might lead to an increase in the pre-exponential factor describing WD kinetics, we must also consider the field effect on the WD activation barrier. In the classic Butler-Volmer model, increasing applied overpotential leads to an increase in electron-transfer rate by lowering activation barrier. The transfer coefficient, typically called α (which can be equated to the symmetry factor of the free-energy surface for elementary reaction steps) [62], is often taken to be 0.5. This assumption is based on the idea that the electron transfer occurs through the width of the double layer (i.e., it is an outer sphere process) and that the free-energy surface is symmetric with respect to approach to the transition state.

While we use a similar formulation to describe the rate of proton transfer in WD, the experimental values for the proton-transfer coefficient α are much smaller, i.e., from 0 to ~0.04, resulting in a weak E_a dependence on η_{wd} for catalyzed BPMs compared with typical electrochemical reactions. The field-dependence of WD has typically been interpreted in context of the second Wien effect by a strong local field that increases the dissociation rate of weak electrolytes, although others have questioned whether a sufficiently strong field in fact exists in the BPM [15,26]. Our new experimental data shed light on this

fundamental process. Increasing electric field, represented by a larger driving force for WD in η_{wd}, does decrease the experimental activation barrier, supporting the field-effect argument. Yet this effect is only significant for BPMs without catalyst that have a narrow junction thickness and hence high electric field (and thus very poor WD/BPM performance).
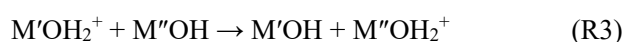
In BPMs, the electric potential drop mainly occurs at the junction, thus the *electric potential drop distance* is roughly the junction thickness. For pristine BPM without catalyst, the junction thickness is ~1–5 nm considering the depletion region, interface roughness, and intermixing between AEL and CEL (**Figure 5b**) [2,63-65]. For a hydrogen bond in liquid water (O–H⋯O), the O–H bond length is ~0.1 nm and the H⋯O bond length is ~0.2 nm [66]. Thus the proton transfer distance for WD ($2H_2O \rightarrow H_3O^+ + OH^-$) is ~0.1 nm. If we take the junction thickness to be ~2 nm, then the ratio between proton-transfer distance and the overall potential-drop distance is ~0.05, which is comparable to the experimental α of pristine BPMs ~0.04; that is, only about 5% of the potential drop across the entire interface is available, on average, to facilitate any given proton transfer.
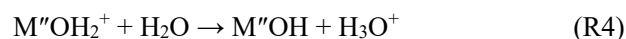
The situation is more complicated when WD catalysts are introduced because the spatial electric-field profile in the junction, especially near the catalyst surface where WD occurs, is unknown. From previous work, the TiO_2-P25 thickness at optimal loading (0.2 wt%) is ~200 nm [24]. Thus the ratio between proton-transfer distance and the overall potential-drop distance is ~0.0004 which is comparable to the experimental α ~0 of optimal loading samples. If the electric field were uniform inside the BPM junction, further increasing the WD catalyst loading and thus junction thickness, should decrease α. However, the experimental result for the much thicker 2 wt% is α ~ 0.002. By adding ACB, α for similar samples increases to ~0.01. This data suggests that the catalyst screens the electric field inside the nanoparticles, thus focusing the electric field outside where WD takes place. Continuum, molecular-dynamics (MD), and density-

functional-theory (DFT) modelling would help test the above hypothesis (see below).

In bulk water, WD occurs through rare electric-field fluctuations and the generated ions recombine quickly if they are not sufficiently separated [67]. This is likely also the case for the pristine BPM without WD catalyst and why it requires a large η_{wd}. The situation is different when there are nanoparticle catalysts where H_2O can transfer H^+ to the oxide surface which can be transported on the nanoparticle surface towards the CEL, while OH^- can be transported in the water "matrix" surrounding the nanoparticles towards the AEL. Thus, one might view the WD catalyst as facilitating the correct configuration of water and surface for successful proton transfer and the WD reaction to occur. Compared to the uncatalyzed BPM, our data shows that adding a WD catalyst leads to a dramatic increase in the driving-force-independent proton-transfer conductance G_0, which can be explained by the large number of sites for proton transfer on the catalyst surface. In the isotope experiment, G_0 follows the same dependence on loading for both H_2O and D_2O, and the ratio $G_0(H_2O)/G_0(D_2O)$ is ~10. This is comparable with the ratio of k_D and K_w (**Table 1**), suggesting that G_0 represents both the number density of catalytic sites and the "intrinsic" WD activity of H_2O and D_2O related to their atomic motions. In the experiment where conducting carbon was added, G_0 does not change because the mass of TiO_2-P25 was kept constant as the mass of carbon was varied. Adding carbon further focuses the electric field, thus WD becomes more sensitive to the change in the electric field, which manifests in the increasing α.
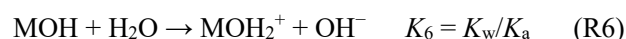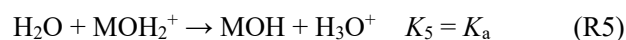
A molecular interpretation of WD catalysis. We propose a molecular proton-transfer mechanism, where M, M′, and M″ denote different proton acceptor/donor sites on the catalyst surface (**Figure 5a**):

$$H_2O + MO^- \rightarrow OH^- + MOH \qquad (R1)$$

$$MOH + M'OH \rightarrow MO^- + M'OH_2^+ \qquad (R2)$$

$$M'OH_2^+ + M''OH \rightarrow M'OH + M''OH_2^+ \qquad (R3)$$

$$M''OH_2^+ + H_2O \rightarrow M''OH + H_3O^+ \qquad\qquad (R4)$$

This mechanism is reminiscent of the basic and acidic two-step mechanism proposed previously [15].

Here we use the acidic two-step mechanism (R5 and R6) for discussion, but the basic case is analogous.

$$H_2O + MOH_2^+ \rightarrow MOH + H_3O^+ \quad K_5 = K_a \qquad (R5)$$

$$MOH + H_2O \rightarrow MOH_2^+ + OH^- \quad K_6 = K_w/K_a \qquad (R6)$$

In the previous two-step mechanisms proposed [15], there is an underlying assumption that the catalytic

cycle occurs on the same site, which means that H_3O^+ and OH^- are produced in close proximity. This

constrains the optimal K_a of the example MOH_2^+ site; if the K_a is large (more acidic), then R5 is more favored

(and usually faster), but this means that R6 is less favored (and usually slower) because its equilibrium

constant is K_w/K_a (if we assume a constant K_w). This is why previous calculations conclude that a pK_a (or

equivalently pK_b) of ~7 of the catalytic site should give the best performance [31].

The new mechanism proposed here involving surface proton transfer (R2 and R3) enables R1 and R4

to occur at different sites (M and M″) on the catalyst surface and thus generate H_3O^+ and OH^- which are

separated in space. The K_a of the M and M″ site are less constrained than in the single-site model. The M

site could be basic so that R1 is favored and fast, while M″ site could be acidic so that R4 is favored and fast,

and the relevant surface K_a will also depend on the degree of polarization of the nanoparticle catalysts [68].

The rate-determining step likely depends on the WD catalyst type, because chemically different surfaces will

have different acid-base behavior and surface proton-absorption isotherms. When the loading is small, R1

or R4 might be rate determining. Since these two steps might be more sensitive to the local electric field, we

might observe a larger α. In contrast, at optimal loading, the surface-transport steps (R2 and R3) might be

rate determining leading to Ohmic behavior ($\alpha = 0$), as the experiment shows. We note that theoretical

calculations find a free-energy barrier of 25 ± 4 kJ mol^{-1} for proton transfer and 32 ± 4 kJ mol^{-1} for

dissociative adsorption on the TiO_2 anatase (101) surface in water [56], values similar to our experimental results.

Conclusion

We developed a membrane-potential-sensing method with two integrated reference electrodes in BPM electrolyzers to directly measure the WD overpotential. Through variable temperature studies and Arrhenius-type analysis with TiO_2-P25 as a model, but effective, WD catalyst, we found that the apparent activation energy E_a only weakly depends on η_{wd} while the pre-exponential factor A is directly proportional to η_{wd}. D_2O requires higher η_{wd} to drive WD than H_2O, but surprisingly the E_a are similar and the higher η_{wd} is due to the lower pre-exponential factor. Electronically conducting acetylene carbon black (ACB) improves the performance by lowering E_a, consistent with a field-focusing effect. We developed a "BPM equation" with three parameters to quantitatively describe the temperature-dependent kinetics and discussed the physical meaning of these parameters. We proposed a new molecular mechanism involving rate-determining proton transfer to/from water and proton transport across the catalyst surface under applied voltage. These findings provide insights into, and inspire new strategies for development of, other electrochemical process where WD is relevant, e.g., alkaline hydrogen evolution reaction and CO_2 electroreduction [22,43,44].

One limitation of the work is the that the proposed BPM equation is semi-empirical. Developing an analytical formalism based on a detailed molecular mechanism remains challenging due to the complexity of the BPM junction and it being a buried interface. A general equation for the current density in a 1-D model is

$$j = F \int_{BPM} \left(k_D c_{H_2O} - k_R c_{H^+} c_{OH^-} \right) dx \tag{9}$$

where k_D and k_R are net dissociation and recombination reaction rate constants, c is the concentration, x is the coordinate perpendicular to the planar 1-D junction. The values for k_D, k_R, and c probably all depend on

x, η_{wd} or electric field, and the details of the catalyst [69,70]. However, there is no experimental data regarding the electric potential/field and H_2O, H^+, and OH^- concentration profiles in the BPM junction. *Operando* measurements of pH, pOH, and electric-field profiles in the BPM junction, perhaps with fluorescent indicators and Stark-effect-based probes, would be valuable [71].

Accurate simulations of the interface molecular and continuum chemistry and physics of the system are also needed [64,72]. MD and DFT calculations to test the various proton-transfer WD reaction mechanisms at nanoparticle/water interface under electric field provide insight into elementary reaction barriers and reaction pathways. We also note that according to the Eyring equation from transition-state theory, the pre-exponential factor A is related to the entropy of activation $\Delta S^{\ddagger}$ [73]. Our observation that A is proportional to η_{wd} may also mean $\Delta S^{\ddagger}$ changes with η_{wd}, these relationships can be elucidated by theory and computation. It also remains unclear whether all the nanoparticles participate in the WD reaction or only those near the AEL and CEL. At the molecular scale, we don't know what sites are active for WD on the surface. We presume the bridging and/or terminal oxo/hydroxyl species are the active sites as proton acceptors or donors, but there may be other WD sites. Molecularly precise analogs would be of value to study.

Nonetheless, the developed BPM equation sets a foundation for WD catalyst development and future fundamental studies. Any theory should reduce to the semi-empirical equation under appropriate assumptions. The BPM equation also does not explicitly separate the forward WD reaction and reverse H^+/OH^- recombination reaction, which may proceed via different mechanisms or with different rate-determining steps. For this, temperature-dependence and kinetic-isotopic-effect experiments for different WD catalysts in both forward and reverse bias (to obtain full polarization curves) is needed, probably using a hydrogen-pump cell instead of a water electrolyzer platform [74].

EXPERIMENTAL PROCEDURES

Resource availability

Lead contact

Further information and request for resources and materials should be directed to and will be fulfilled by the lead contact, Shannon Boettcher (swb@uoregon.edu).

Materials availability

Bipolar membranes created in this study are available by reasonable request from the lead author.

Data and code availability.

The data presented in this work are available from the corresponding author upon reasonable request and will be deposited in the Science Data Bank (https://www.scidb.cn/en).

Bipolar membrane fabrication and measurements. The experimental procedures are modified from our previous report [24]. The anode gas-diffusion electrode/layer (GDE/GDL) was fabricated by spray coating two vials of anode inks (dispersed by sonication), containing 0.1 g Co_3O_4 (30–50 nm, US Research Nanomaterials, Inc.), 0.5 g H_2O, 1.7 g isopropyl alcohol (IPA), and 0.1 g PiperION-A5 Ionomer Suspension (TP-85, 5% w/w, Versogen), onto a 5 cm × 5 cm stainless steel 25AL3 (Bekaert Bekipor®) support taped on a hot plate of 90 °C. The loading was ~2 mg cm^{-2}. Then PiperION-A5 ionomer suspension (as received) was sprayed onto the catalysts until the mass of the ionomer reached 10%–20% of the catalyst mass. The GDL was cut into 1.0 cm × 1.0 cm coupons. The cathode GDL was fabricated in a similar way with Toray Carbon Paper 090 (wet proofed, Fuel Cell Store) as the substrate, and two vials of ink containing 0.1 g Pt black (high surface area, Fuel Cell Store), 1.5 g H_2O, 1.7 g IPA, 0.1 g D520 Nafion™ dispersion (alcohol-based 1000 EW at 5 wt%, Fuel Cell Store).

PiperION-A40-HCO3 (TP-85, 40-μm thick, Versogen) membrane was soaked in 0.5 M KOH for > 1 h,

stored in fresh 0.5 M KOH, and rinsed in ultrapure H_2O before being used as the anion exchange layer (AEL). The Nafion™ 212 (Fuel Cell Store) membrane was soaked and stored in H_2O and used as the cation exchange layer (CEL). Both membranes are cut into 1.5 cm × 1.5 cm for use as the AEL and CEL in the BPM, and 1.5 cm × 7.5 cm as the AEL and CEL sensing strips. The WD catalyst was spin-coated onto the CEL. TiO_2-P25 (Aeroxide® Nippon Aerosil Co., Ltd.) was dispersed in a H_2O/IPA mixture (1:1 by weight) with different wt% solids to make the ink. The edges of a CEL (1.5 cm × 1.5 cm) were taped on a glass slide. The ink was added onto CEL until fully covered and then the sample spun at 3000 rpm for 30 s to create a uniform thin layer of WD catalyst.

Due to the poor dispersibility of acetylene carbon black (ACB), spin coating does not give good quality catalyst coating. Therefore, spray coating was used. A 2 wt% mother ink of TiO_2-P25 was prepared in water and sonicated until well dispersed. Based on the target mass ratio of ACB and TiO_2-P25, ACB was weighed in a 20 mL vial (e.g., 50 wt% required 2 mg of ACB), then 200 mg of the 2 wt% TiO_2-P25 mother ink (equivalent to 4 mg of TiO_2-P25) is added. Water is added until the total mass reaches 0.5 g, then 1.7 g of IPA is added and the mixture is sonicated until well dispersed. A CEL of 1.5 cm × 1.5 cm is taped on a petri dish and placed on a hot plate of 90 °C. The ink is spray coated onto the CEL. To improve the uniformity, the dish is rotated 90° every 10 spray bursts. After spraying, the tapes were removed and the coated CEL was moved into pure water for later use.

The electrolyzer uses PEM fuel-cell hardware (Fuel Cell Store) with the original graphite anode flow field replaced by a homemade stainless-steel one. For step-by-step procedures regarding cell construction and assembly, see the "Supporting Information: Photographs and set-by-step procedure to assemble membrane-potential-sensing system". Ultrapure H_2O (18.2 MΩ cm) heated at different temperatures was fed to both the anode and cathode so that the electrolyzer temperature was 25, 35, 45, or 55 ± 2 °C (error

estimated as the maximum fluctuation). D$_2$O (99.9%, Cambridge Isotope Laboratories) is used instead of H$_2$O for kinetic-isotope effect experiments. Conventionally, Ag|AgCl reference electrodes are usually used measure WD voltage of BPMs in H-cells, but the frits dissolve in strong base and the potentials are unreliable due to formation of AgO. We used a saturated calomel electrode (SCE) in 0.1 M H$_2$SO$_4$ and a Hg|HgO reference electrode (RE) in 0.1 M KOH. The WD voltage V_{wd} was then measured as $V_{wd} = V_{wd}^{raw} + \Delta V_{RE}$, where V_{wd}^{raw} is the as-measured voltage between Hg|HgO and SCE during test, and $\Delta V_{RE} = 0.136$ V (measured in saturated KCl solution) is the correction factor for the difference between Hg|HgO and SCE in the same solution at equilibrium without the effect of transmembrane voltages. To calculate η_{wd}, it is not strictly necessary to correct for ΔV_{RE} as

$$\eta_{wd} \equiv V_{wd} - V_{wd,eq} = (V_{wd}^{raw} + \Delta V_{RE}) - (V_{wd,eq}^{raw} + \Delta V_{RE}) = V_{wd}^{raw} - V_{wd,eq}^{raw} \qquad (10)$$

where the subscript "eq" denotes the equilibrium value, i.e., when current density $j = 0$ mA cm^{-2}.

The electrochemical tests were performed with a two-channel BioLogic VSP-300 potentiostat. For channel 1, the P1 and S1 leads were connected to the anode current collector, P2, S2 and S3 were connected to the cathode current collector (P = power lead, S = sense lead). For channel 2, S1 was connected to the Hg|HgO RE, S2 to the cathode current collector, and S3 to the SCE RE. P1 and P2 were not used. Channel 1 and channel 2 are synchronized during the experiment. Channel 2 records voltage every 0.1 s. The current was applied by Channel 1 and stepped up at j = 10, 50, 100, 150, …, 500 mA cm^{-2} (10 s each step) and held at 500 mA cm^{-2} for 10 min (if the voltage exceeds the maximum range of the potentiostat, then held at the highest j). Then galvanostatic electrochemical impedance spectroscopy (GEIS) was measured from 600 kHz to 60 mHz with four points per decade at 500, 450, 400, …, 100, 50, 40, 30, 20, 10, 5 mA cm^{-2} with an AC amplitude of 6% of the applied DC current density (for 10 and 5 mA cm^{-2}, an amplitude of 1 mA cm^{-2} was used). The impedance data were fit with impedance.py [75]. The $R(j)$ plot is extrapolated by cubic spline to j =

0 mA cm^{-2} so that the integral $\eta_{\text{wd}} = \int_0^j R_{\text{wd}}(j)\mathrm{d}j$ begins at 0. For the temperature-dependent tests, after GEIS, j was stepped up again (5 s each step) and held at 500 mA cm^{-2} for 2 min. Then j was stepped down at 500, 450, 400, …, 100, 50, 40, 30, 20, 10, 5 mA cm^{-2} (5 s each step). The last three seconds of each step was averaged to produce the polarization curves. For the BPM without catalyst, j was decreased by a factor of 100 to prevent large voltage polarizations. The temperature was then changed, and the procedure repeated. Temperatures from 25 to 55 °C (every 10 °C) and back to 25 °C were used. Two temperature cycles were performed for each test. A degradation (increase in voltage) was sometimes observed in the first temperature step up process for low-catalyst-loading samples, after which the performance (at the same temperature) was repeatable during cycling. Thus, the first 25, 35, and 45 °C data were not used for the temperature-dependence analysis for those samples (**Figure S2**).

SUPPLEMENTAL INFORMATION

Temperature-dependent WD polarization curves for BPMs with different loadings of TiO$_2$-P25 as WD catalyst; measured WD overpotential η_{wd} using electrochemical impedance spectroscopy (EIS); correction of degradation over time for a pristine, uncatalyzed BPM; kinetic isotope effect; Arrhenius analysis of the temperature-dependent polarization curves of BPMs with different mass ratio of ACB and TiO$_2$-P25; photographs and set-by-step procedure to assemble membrane-potential-sensing system.

AUTHOR CONTRIBUTIONS

S.W.B. conceived the experiments and led the project. L.C. performed most experiments. Q.X. and L.C.

performed pilot experiments. L.C. and S.W.B. wrote the manuscript with input from all authors.

DECLARATION OF INTERESTS

The Authors have filed a provisional patent on aspects of the work.

References

1. Giesbrecht, P.K., and Freund, M.S. (2020). Recent Advances in Bipolar Membrane Design and Applications. Chem. Mater. *32*, 8060-8090. 10.1021/acs.chemmater.0c02829.
2. Pärnamäe, R., Mareev, S., Nikonenko, V., Melnikov, S., Sheldeshov, N., Zabolotskii, V., Hamelers, H.V.M., and Tedesco, M. (2021). Bipolar membranes: A review on principles, latest developments, and applications. J. Membr. Sci. *617*, 118538. https://doi.org/10.1016/j.memsci.2020.118538.
3. Blommaert, M.A., Aili, D., Tufa, R.A., Li, Q., Smith, W.A., and Vermaas, D.A. (2021). Insights and Challenges for Applying Bipolar Membranes in Advanced Electrochemical Energy Systems. ACS Energy Lett. *6*, 2539-2548. 10.1021/acsenergylett.1c00618.
4. Yan, Z., and Mallouk, T.E. (2021). Bipolar Membranes for Ion Management in (Photo)Electrochemical Energy Conversion. Accounts of Materials Research *2*, 1156-1166. 10.1021/accountsmr.1c00113.
5. Miesiac, I., and Rukowicz, B. (2022). Bipolar Membrane and Water Splitting in Electrodialysis. Electrocatalysis *13*, 101-107. 10.1007/s12678-021-00703-5.
6. Strathmann, H. (2010). Electrodialysis, a Mature Technology With a Multitude of New Applications. Desalination *264*, 268-288. 10.1016/j.desal.2010.04.069.
7. Shehzad, M.A., Yasmin, A., Ge, X., Ge, Z., Zhang, K., Liang, X., Zhang, J., Li, G., Xiao, X., Jiang, B., et al. (2021). Shielded Goethite Catalyst that Enables Fast Water Dissociation in Bipolar Membranes. Nat. Commun. *12*, 9. 10.1038/s41467-020-20131-1.
8. Fu, R., Wang, H., Yan, J., Li, R., Jiang, C., Wang, Y., and Xu, T. (2022). Asymmetric Bipolar Membrane Electrodialysis for Acid and Base Production. AIChE J. *n/a*, e17957. 10.1002/aic.17957.
9. Lu, H., Wang, L., Wycisk, R., Pintauro, P.N., and Lin, S. (2020). Quantifying the Kinetics-Energetics Performance Tradeoff in Bipolar Membrane Electrodialysis. J. Membr. Sci. *612*, 118279. 10.1016/j.memsci.2020.118279.
10. Bazinet, L., Lamarche, F., and Ippersiel, D. (1998). Bipolar-Membrane Electrodialysis: Applications of Electrodialysis in the Food Industry. Trends Food Sci. Technol. *9*, 107-113. 10.1016/S0924-2244(98)00026-0.
11. Tongwen, X. (2002). Electrodialysis processes with bipolar membranes (EDBM) in environmental protection—a review. Resources, Conservation and Recycling *37*, 1-22. https://doi.org/10.1016/S0921-3449(02)00032-0.

12. Ahlfield, J.M., Liu, L., and Kohl, P.A. (2017). PEM/AEM junction design for bipolar membrane fuel cells. J. Electrochem. Soc. *164*, F1165-F1171. 10.1149/2.1041712jes.

13. Peng, S., Xu, X., Lu, S., Sui, P.-C., Djilali, N., and Xiang, Y. (2015). A Self-Humidifying Acidic–Alkaline Bipolar Membrane Fuel Cell. J. Power Sources *299*, 273-279. 10.1016/j.jpowsour.2015.08.104.

14. Yan, Z., Wycisk, R.J., Metlay, A.S., Xiao, L., Yoon, Y., Pintauro, P.N., and Mallouk, T.E. (2021). High-Voltage Aqueous Redox Flow Batteries Enabled by Catalyzed Water Dissociation and Acid–Base Neutralization in Bipolar Membranes. ACS Central Science *7*, 1028-1035. 10.1021/acscentsci.1c00217.

15. Oener, S.Z., Foster, M.J., and Boettcher, S.W. (2020). Accelerating Water Dissociation in Bipolar Membranes and for Electrocatalysis. Science *369*, 1099-1103. 10.1126/science.aaz1487.

16. Powers, D., Mondal, A.N., Yang, Z., Wycisk, R., Kreidler, E., and Pintauro, P.N. (2022). Freestanding Bipolar Membranes with an Electrospun Junction for High Current Density Water Splitting. ACS Appl. Mater. Interfaces *14*, 36092-36104. 10.1021/acsami.2c07680.

17. Kibsgaard, J., and Chorkendorff, I. (2019). Considerations for the scaling-up of water splitting catalysts. Nat. Energy. *4*, 430-433. 10.1038/s41560-019-0407-1.

18. Xie, K., Miao, R.K., Ozden, A., Liu, S., Chen, Z., Dinh, C.-T., Huang, J.E., Xu, Q., Gabardo, C.M., Lee, G., et al. (2022). Bipolar membrane electrolyzers enable high single-pass CO_2 electroreduction to multicarbon products. Nature Communications *13*, 3609. 10.1038/s41467-022-31295-3.

19. Blommaert, M.A., Sharifian, R., Shah, N.U., Nesbitt, N.T., Smith, W.A., and Vermaas, D.A. (2021). Orientation of a bipolar membrane determines the dominant ion and carbonic species transport in membrane electrode assemblies for CO2 reduction. Journal of Materials Chemistry A *9*, 11179-11186. 10.1039/D0TA12398F.

20. Marin, D.H., Perryman, J.T., Hubert, M.A., Lindquist, G.A., Chen, L., Aleman, A.M., Kamat, G.A., Niemann, V.A., Stevens, M.B., Boettcher, S.W., et al. (2023). Hydrogen Production with Seawater-Resilient Bipolar-Membrane Electrolyzers. Joule *in review*.

21. Subbaraman, R., Tripkovic, D., Strmcnik, D., Chang, K.C., Uchimura, M., Paulikas, A.P., Stamenkovic, V., and Markovic, N.M. (2011). Enhancing hydrogen evolution activity in water splitting by tailoring Li^+-$Ni(OH)_2$-Pt interfaces. Science *334*, 1256-1260. 10.1126/science.1211934.

22. McCrum, I.T., and Koper, M.T.M. (2020). The Role of Adsorbed Hydroxide in Hydrogen Evolution Reaction Kinetics on Modified Platinum. Nat. Energy. *5*, 891-899. 10.1038/s41560-020-00710-8.

23. Marcandalli, G., Monteiro, M.C.O., Goyal, A., and Koper, M.T.M. (2022). Electrolyte Effects on CO2 Electrochemical Reduction to CO. Acc. Chem. Res. *55*, 1900-1911. 10.1021/acs.accounts.2c00080.

24. Chen, L., Xu, Q., Oener, S.Z., Fabrizio, K., and Boettcher, S.W. (2022). Design principles for water dissociation catalysts in high-performance bipolar membranes. Nature Communications *13*, 3846. 10.1038/s41467-022-31429-7.

25. Onsager, L. (1934). Deviations from Ohm's law in weak electrolytes. J. Chem. Phys. *2*, 599-615. 10.1063/1.1749541.

26. Kunst, B., and Lovreček, B. (1962). Electrochemical Properties of the Ion-Exchange Membranes Junction. II. Croat. Chem. Acta *34*, 219-229.

27. Cai, J., Griffin, E., Guarochico-Moreira, V.H., Barry, D., Xin, B., Yagmurcukardes, M., Zhang, S., Geim, A.K., Peeters, F.M., and Lozada-Hidalgo, M. (2022). Wien Effect in Interfacial Water Dissociation Through Proton-Permeable Graphene Electrodes. Nat. Commun. *13*, 5776. 10.1038/s41467-022-33451-1.

28. Cai, J., Griffin, E., Guarochico-Moreira, V., Barry, D., Xin, B., Huang, S., Geim, A.K., Peeters, F.M., and Lozada-Hidalgo, M. (2022). Photoaccelerated Water Dissociation Across One-Atom-Thick Electrodes.

Nano Lett. *22*, 9566-9570. 10.1021/acs.nanolett.2c03701.

29. Simons, R., and Khanarian, G. (1978). Water dissociation in bipolar membranes: experiments and theory. J. Membrane Biol. *38*, 11-30. 10.1007/BF01875160.

30. Simons, R. (1979). Strong electric field effects on proton transfer between membrane-bound amines and water. Nature *280*, 824-826. 10.1038/280824a0.

31. Strathmann, H., Krol, J.J., Rapp, H.J., and Eigenberger, G. (1997). Limiting current density and water dissociation in bipolar membranes. J. Membr. Sci. *125*, 123-142. 10.1016/s0376-7388(96)00185-8.

32. Yan, Z., Zhu, L., Li, Y.C., Wycisk, R.J., Pintauro, P.N., Hickner, M.A., and Mallouk, T.E. (2018). The balance of electric field and interfacial catalysis in promoting water dissociation in bipolar membranes. Energy & Environmental Science *11*, 2235-2245. 10.1039/C8EE01192C.

33. Ramírez, P., Rapp, H.J., Reichle, S., Strathmann, H., and Mafé, S. (1992). Current‐Voltage Curves of Bipolar Membranes. J. Appl. Phys. *72*, 259-264. 10.1063/1.352124.

34. Aritomi, T., van den Boomgaard, T., and Strathmann, H. (1996). Current-Voltage Curve of a Bipolar Membrane at High Current Density. Desalination *104*, 13-18. 10.1016/0011-9164(96)00021-5.

35. Hurwitz, H.D., and Dibiani, R. (2001). Investigation of Electrical Properties of Bipolar Membranes at Steady State and With Transient Methods. Electrochim. Acta *47*, 759-773. 10.1016/S0013-4686(01)00757-5.

36. Hurwitz, H.D., and Dibiani, R. (2004). Experimental and Theoretical Investigations of Steady and Transient States in Systems of Ion Exchange Bipolar Membranes. J. Membr. Sci. *228*, 17-43. 10.1016/j.memsci.2003.09.009.

37. He, Z.-D., Chen, Y.-X., Santos, E., and Schmickler, W. (2018). The Pre-exponential Factor in Electrochemistry. Angew. Chem. Int. Ed. *57*, 7948-7956. 10.1002/anie.201800130.

38. Oener, S.Z., Twight, L.P., Lindquist, G.A., and Boettcher, S.W. (2021). Thin Cation-Exchange Layers Enable High-Current-Density Bipolar Membrane Electrolyzers via Improved Water Transport. ACS Energy Lett. *6*, 1-8. 10.1021/acsenergylett.0c02078.

39. Xu, Q., Oener, S.Z., Lindquist, G., Jiang, H., Li, C., and Boettcher, S.W. (2021). Integrated Reference Electrodes in Anion-Exchange-Membrane Electrolyzers: Impact of Stainless-Steel Gas-Diffusion Layers and Internal Mechanical Pressure. ACS Energy Lett. *6*, 305-312. 10.1021/acsenergylett.0c02338.

40. Adler, S.B. (2002). Reference Electrode Placement in Thin Solid Electrolytes. J. Electrochem. Soc. *149*, E166. 10.1149/1.1467368.

41. He, W., and Nguyen, T.V. (2004). Edge Effects on Reference Electrode Measurements in PEM Fuel Cells. J. Electrochem. Soc. *151*, A185. 10.1149/1.1634272.

42. Zeng, R., Slade, R.C.T., and Varcoe, J.R. (2010). An Experimental Study on The Placement of Reference Electrodes in Alkaline Polymer Electrolyte Membrane Fuel Cells. Electrochim. Acta *56*, 607-619. 10.1016/j.electacta.2010.08.032.

43. Intikhab, S., Snyder, J.D., and Tang, M.H. (2017). Adsorbed Hydroxide Does Not Participate in the Volmer Step of Alkaline Hydrogen Electrocatalysis. ACS Catal. *7*, 8314-8319. 10.1021/acscatal.7b02787.

44. Huang, B., Rao, R.R., You, S., Hpone Myint, K., Song, Y., Wang, Y., Ding, W., Giordano, L., Zhang, Y., Wang, T., et al. (2021). Cation- and pH-Dependent Hydrogen Evolution and Oxidation Reaction Kinetics. JACS Au *1*, 1674-1687. 10.1021/jacsau.1c00281.

45. Eigen, M., and Maeyer, L.d. (1955). Untersuchungen über die kinetik der neutralisation. I. Z. Elektrochem. *59*, 986. 10.1002/bbpc.19550591020.

46. Eigen, M., De Maeyer, L., and Bernal, J.D. (1958). Self-Dissociation and Protonic Charge Transport in Water and Ice. Proceedings of the Royal Society of London. Series A: Mathematical and Physical

Sciences *247*, 505-533. 10.1098/rspa.1958.0208.

47. Natzle, W.C., and Moore, C.B. (1985). Recombination of Hydrogen Ion (H$^+$) and Hydroxide in Pure Liquid Water. The Journal of Physical Chemistry *89*, 2605-2612. 10.1021/j100258a035.

48. Sweeton, F.H., Mesmer, R.E., and Baes, C.F. (1974). Acidity Measurements at Elevated Temperatures. VII. Dissociation of Water. J. Solution Chem. *3*, 191-214. 10.1007/BF00645633.

49. Shoesmith, D.W., and Lee, W. (1976). The Ionization Constant of Heavy Water (D$_2$O) in the Temperature Range 298 to 523 K. Can. J. Chem. *54*, 3553-3558. 10.1139/v76-511.

50. Ertl, G., and Gerischer, H. (1962). Ein vergleich der kinetik der neutralisationsreaktionen des leichten und schweren wassers. Z. Elecktrochem. *66*, 560.

51. Mills, R. (1973). Self-Diffusion in Normal and Heavy Water in the Range 1-45°. The Journal of Physical Chemistry *77*, 685-688. 10.1021/j100624a025.

52. CRC Handbook of Chemistry and Physics: A Ready-Reference Book of Chemical and Physical Data. (2017). 97th Edition (CRC Press Boca Raton).

53. Lee, S.H., and Rasaiah, J.C. (2011). Proton Transfer and the Mobilities of the H$^+$ And OH$^-$ Ions From Studies of a Dissociating Model for Water. J. Chem. Phys. *135*, 124505. 10.1063/1.3632990.

54. Gierer, A. (1950). Anomale D+ -und OD– -Ionenbeweglichkeit in Schwerem Wasser. Zeitschrift für Naturforschung A *5*, 581-589. 10.1515/zna-1950-1102.

55. Bourikas, K., Kordulis, C., and Lycourghiotis, A. (2014). Titanium Dioxide (Anatase and Rutile): Surface Chemistry, Liquid–Solid Interface Chemistry, and Scientific Synthesis of Supported Catalysts. Chem. Rev. *114*, 9754-9823. 10.1021/cr300230q.

56. Calegari Andrade, M.F., Ko, H.-Y., Zhang, L., Car, R., and Selloni, A. (2020). Free Energy of Proton Transfer at the Water–TiO$_2$ Interface From *ab initio* Deep Potential Molecular Dynamics. Chem. Sci. *11*, 2335-2341. 10.1039/C9SC05116C.

57. Bockris, J.O.M., Devanathan, M.A.V., and Müller, K. (1963). On the Structure of Charged Interfaces. Proceedings of the Royal Society of London. Series A: Mathematical and Physical Sciences *274*, 55-79.

58. Willard, A.P., Reed, S.K., Madden, P.A., and Chandler, D. (2009). Water at an Electrochemical Interface—A Simulation Study. Faraday Discuss. *141*, 423-441. 10.1039/B805544K.

59. Gonella, G., Backus, E.H.G., Nagata, Y., Bonthuis, D.J., Loche, P., Schlaich, A., Netz, R.R., Kühnle, A., McCrum, I.T., Koper, M.T.M., et al. (2021). Water at Charged Interfaces. Nature Reviews Chemistry *5*, 466-485. 10.1038/s41570-021-00293-2.

60. Fosdick, S.E., Knust, K.N., Scida, K., and Crooks, R.M. (2013). Bipolar Electrochemistry. Angew. Chem. Int. Ed. *52*, 10438-10456. 10.1002/anie.201300947.

61. Guerrero García, G.I., and Olvera de la Cruz, M. (2014). Polarization Effects of Dielectric Nanoparticles in Aqueous Charge-Asymmetric Electrolytes. J. Phys. Chem. B *118*, 8854-8862. 10.1021/jp5045173.

62. Bockris, J.O.M., and Nagy, Z. (1973). Symmetry Factor and Transfer Coefficient: A Source of Confusion in Electrode Kinetics. J. Chem. Educ. *50*, 839. 10.1021/ed050p839.

63. Wrubel, J.A., Chen, Y., Ma, Z., and Deutsch, T.G. (2020). Modeling Water Electrolysis in Bipolar Membranes. J. Electrochem. Soc. *167*, 114502. 10.1149/1945-7111/ab9ccb.

64. Bui, J.C., Digdaya, I., Xiang, C., Bell, A.T., and Weber, A.Z. (2020). Understanding Multi-Ion Transport Mechanisms in Bipolar Membranes. ACS Appl. Mater. Interfaces *12*, 52509-52526. 10.1021/acsami.0c12686.

65. Mareev, S.A., Evdochenko, E., Wessling, M., Kozaderova, O.A., Niftaliev, S.I., Pismenskaya, N.D., and Nikonenko, V.V. (2020). A Comprehensive Mathematical Model of Water Splitting in Bipolar Membranes: Impact of the Spatial Distribution of Fixed Charges and Catalyst at Bipolar Junction. J.

Membr. Sci. *603*, 118010. 10.1016/j.memsci.2020.118010.

66. Chen, B., Ivanov, I., Klein, M.L., and Parrinello, M. (2003). Hydrogen Bonding in Water. Phys. Rev. Lett. *91*, 215503. 10.1103/PhysRevLett.91.215503.

67. Geissler, P.L., Dellago, C., Chandler, D., Hutter, J., and Parrinello, M. (2001). Autoionization in liquid water. Science *291*, 2121-2124. 10.1126/science.1056991.

68. Delley, M.F., Nichols, E.M., and Mayer, J.M. (2021). Interfacial Acid–Base Equilibria and Electric Fields Concurrently Probed by *in situ* Surface-Enhanced Infrared Spectroscopy. J. Am. Chem. Soc. *143*, 10778-10792. 10.1021/jacs.1c05419.

69. Stuve, E.M. (2012). Ionization of water in interfacial electric fields: An electrochemical view. Chem. Phys. Lett. *519-520*, 1-17. 10.1016/j.cplett.2011.09.040.

70. Che, F., Gray, J.T., Ha, S., Kruse, N., Scott, S.L., and McEwen, J.-S. (2018). Elucidating the Roles of Electric Fields in Catalysis: A Perspective. ACS Catal. *8*, 5153-5174. 10.1021/acscatal.7b02899.

71. Yan, Z., Hitt, J.L., Zeng, Z., Hickner, M.A., and Mallouk, T.E. (2021). Improving the Efficiency of CO_2 Electrolysis by Using a Bipolar Membrane With a Weak-Acid Cation Exchange Layer. Nat. Chem. *13*, 33-40. 10.1038/s41557-020-00602-0.

72. Bui, J.C., Corpus, K.R.M., Bell, A.T., and Weber, A.Z. (2021). On the Nature of Field-Enhanced Water Dissociation in Bipolar Membranes. J. Phys. Chem. C *125*, 24974-24987. 10.1021/acs.jpcc.1c08276.

73. Doyle, P.J., Savara, A., and Raiman, S.S. (2020). Extracting Meaningful Standard Enthalpies and Entropies of Activation for Surface Reactions From Kinetic Rates. Reaction Kinetics, Mechanisms and Catalysis *129*, 551-581. 10.1007/s11144-020-01747-2.

74. Mitchell, J.B., Chen, L., Langworthy, K., Fabrizio, K., and Boettcher, S.W. (2022). Catalytic Proton–Hydroxide Recombination for Forward-Bias Bipolar Membranes. ACS Energy Lett. *7*, 3967-3973. 10.1021/acsenergylett.2c02043.

75. Murbach, M.D., Gerwe, B., Dawson-Elli, N., and Tsui, L.-k. (2020). Impedance.py: A Python Package for Electrochemical Impedance Analysis. Journal of Open Source Software *5*, 2349. 10.21105/joss.02349.